JACS Au
AN OPEN ACCESS JOURNAL OF THE AMERICAN CHEMICAL SOCIETY

pubs.acs.org/jacsau
Article

Proton Tunneling Allows a Proton-Coupled Electron Transfer Process in the Cancer Cell

Tong Zhang,‡ Arindam Ghosh,‡ Lisa Behringer-Pließ, Lata Chouhan, Ana V. Cunha, Remco W. A. Havenith, Eugenia Butkevich, Lei Zhang, Olalla Vázquez, Elke Debroye, Jörg Enderlein,* and Shoubhik Das*

Cite This: JACS Au 2024, 4, 4856−4865
Read Online

ACCESS | Metrics & More | Article Recommendations | Supporting Information

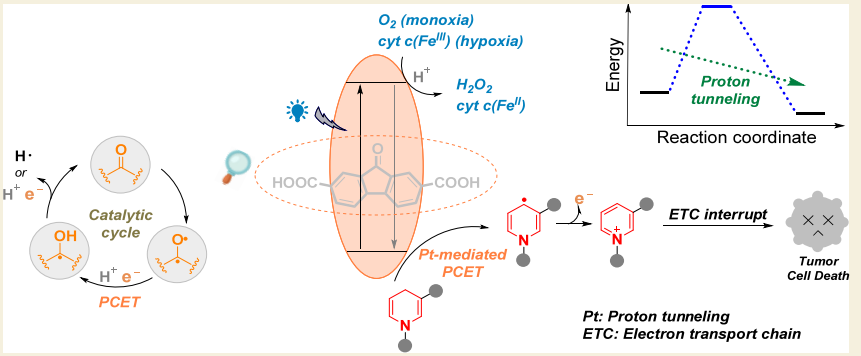

ABSTRACT: Proton-coupled electron transfer (PCET) is a fundamental redox process and has clear advantages in selectively activating challenging C−H bonds in many biological processes. Intrigued by this activation process, we aimed to develop a facile PCET process in cancer cells by modulating proton tunneling. This approach should lead to the design of an alternative photodynamic therapy (PDT) that depletes the mitochondrial electron transport chain (ETC), the key redox regulator in cancer cells under hypoxia. To observe this depletion process in the cancer cell, we monitored the oxidative-stress-induced depolarization of mitochondrial inner membrane potential (MMP) using fluorescence lifetime imaging microscopy (FLIM). Typically, increasing metabolic stress of cancer cells is reflected in a nontrivial change in the fluorophore's fluorescence lifetime. After 30 min of irradiation, we observed a shift in the mean lifetime value and a drastic drop in overall fluorescence signal. In addition, our PCET strategy resulted in drastic reorganization of mitochondrial morphology from tubular to vesicle-like and causing an overall depletion of intact mitochondria in the hypodermis of *C. elegans*. These observations confirmed that PCET promoted ROS-induced oxidative stress. Finally, we gained a clear understanding of the proton tunneling effect in the PCET process through photoluminescence experiments and DFT calculations.

KEYWORDS: *proton tunneling, proton-coupled electron transfer, photodynamic therapy, metal free, fluorenone derivatives*

Proton-coupled electron transfer (PCET) is a well-known fundamental redox process where a proton and electron are simultaneously transferred to the respective proton and electron accepting site.[1,2] However, it is unclear whether the PCET occurs as a concerted process without intermediate formation or as a multistep pathway where either the electron (ET = Electron Transfer) or the proton (PT = Proton Transfer) relocates in two separate steps. Nevertheless, the total Gibb's free energy (ΔG_{PCET}) is considerably more negative than its values for the individual processes (ΔG_{ET} or ΔG_{PT}).[3−6] In this context, it should be noted that the rapid proton tunneling results in faster rates of PCET, which affects catalysis. However, this tunneling does not alter the thermodynamic characteristics of the respective chemical reactions; rather, it enhances PT if it is involved in the rate-determining step.[7−11] Notably, PCET behaves similarly to traditional hydrogen atom transfer (HAT). However, PCET has clear advantages for the activation of many organic molecules that are impossible to achieve via HAT.[12,13] In particular, simultaneous breaking and formation of bonds via HAT must always be considered, with regard to the respective bond strengths. This could be a significant drawback when cleaving a particularly strong bond, which makes the design of robust HAT-mediated strategies challenging. For example, many protic functional groups such as alcohols or amines have

Received: September 4, 2024
Revised: October 16, 2024
Accepted: October 17, 2024
Published: December 10, 2024

https://doi.org/10.1021/jacsau.4c00815
JACS Au 2024, 4, 4856−4865

Scheme 1. Photodynamic Therapy Using PCET

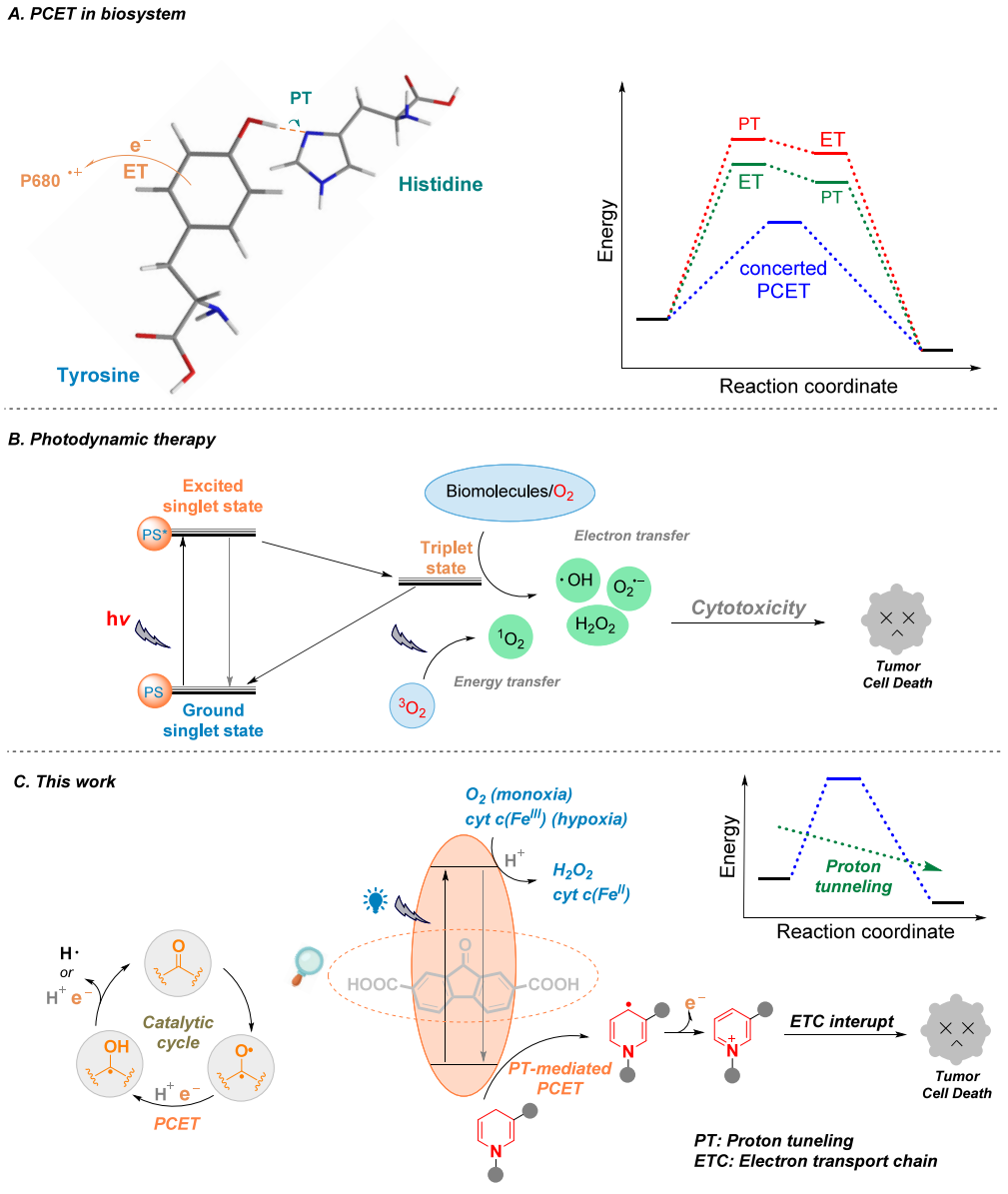

bond strengths of more than 100 kcal mol^{-1}, which is certainly quite high for designing a robust HAT reagent. If these bond strengths are provided by the HAT reagent, this could create additional selectivity issues inside the molecule due to the presence of weaker bonds.[14,15] Considering all these factors, PCET is an energetically less demanding process and plays many key roles in biological processes such as photosynthesis, enzymatic catalysis, respiration, nitrogen fixation, and many others (Scheme 1A).[16,17]

Photodynamic therapy (PDT) has emerged as an alternative treatment for cancer patients (Scheme 1B). PDT requires a photosensitizer that, under the light irradiation, generates an excited singlet state.[18−22] After formation of this singlet excited state, there are two possibilities: (i) relaxation to the ground state and (ii) intersystem crossing into a less energetic triplet excited state.[23−25] Due to the relatively longer lifetime[26,27] as well as the spin angular momentum conservation,[28] PDT proceeds efficiently via the triplet excited state, generating reactive oxygen species (ROS) such as hydroxy radicals (·OH), superoxide radical anions ($O_2^{\bullet-}$), or singlet oxygen molecules ($^1O_2$). While highly reactive hydroxy radicals are immediately quenched through interacting with biomolecules at the site of their formation, singlet oxygen plays the key role as a ROS in the PDT, due to the fast reaction rate constant of ≈1−3 × 10^9 M^{-1} s^{-1} for singlet oxygen generation (fast as compared to electron transfer processes with reaction rate constants smaller than 1 × 10^7 M^{-1} s^{-1}).[29−31] From this comparison, it becomes clear that the presence of oxygen is essential for designing an efficient PDT, although most of cancer cells grow under hypoxia (oxygen is not available in sufficient amounts).[32] Indeed, there exists several strategies for enhancing the effect of PDT under hypoxia; however, for instance, in type-I PDT, despite the lower demand for oxygen, type-I photosensitizers still necessitate interaction with O_2, which can be supplemented through the subsequent reaction process.[33−35] Thus, the design of alternative PDTs that work efficiently in the absence of oxygen or under low concentration of oxygen is highly desirable.[36,37] For these alternative PDTs, the mitochondrial electron transport chain (ETC), which essential for the redox regulation in cancer cells under hypoxia, is depleted via the disruption of 1,4-

https://doi.org/10.1021/jacsau.4c00815
JACS Au 2024, 4, 4856−4865

dihydronicotinamide adenine dinucleotide (NADH).[38−41] In general, NADH acts as the key electron source in the ETC, so that its depletion directly affects the redox reactivity in cancer cells. In this way, cancer cells are destroyed in a highly selective manner under hypoxia. In particular, this route requires one to consider an alternative oxidant such as cytochrome c (cyt c), a heme protein that is localized in the compartment between the inner and outer mitochondrial membranes. Notably, the redox activity of cyt c is attributed to the presence of an iron (Fe) atom in the porphyrin ring, and the transfer of electrons between cyt c and its redox partners involves the conversion between ferrous (Fe^{II}) and ferric (Fe^{III}) forms.[42−44]

Recently conducted detailed investigations of the NADH:ubiquinone oxidoreductase-mediated PCET triggered our interest in designing a PCET-based depletion approach for cancer therapy.[45] Particularly, a remarkable charge-transfer process between NADH and a protein-bound flavin (FMN) cofactor was initiated via an ET between the aromatic ring systems of the cofactors. Inspired by this insight, we aimed to design a PCET-based photocatalyst that could trigger the depletion of NADH in cancer cells (Scheme 1C). The previous observation of the prevalence of carbonyl functionalities in PCET has led us to consider them as potential photocatalysts for this process.[45] In particular, the generation of ketyl radicals through PCET is more energetically favorable than the one-electron reduction of carbonyl groups to generate ketyl radicals through outer-sphere electron transfer.[46] In addition, due to the relatively weak O−H bond in ketyl radicals, they can serve as a source of H• and can subsequently return to carbonyl groups. Moreover, PCET is enhanced by the presence of a carboxylic acid functional, which lead us to surmise that the direct installation of this functional group in the photocatalyst could be beneficial for the depletion of the NADH moiety.[47] In general, the acid group plays a crucial role in facilitating a mechanism that involves hydrogen atom transfer at a distinct oxygen atom, resulting in a degenerate isomerization process and unstrained transition state. This mechanism is also observed in carboxylic acid dimers, where it is responsible for proton tunneling. This, in turn, facilitates the transfer of protons from NADH to the photocatalyst.[48,49] Additionally, the presence of carboxylic acid functional groups can modulate solubility and lipophilicity.[50] For observing PCET in cancer cells, we utilized fluorescence lifetime imaging microscopy (FLIM) of mitochondria.[51] In fact, previous reports demonstrated that changes in the excited-state fluorescence lifetime (FLT) can directly report on mitochondrial membrane potential variations, which are correlated with the cellular metabolic state.[52] Particularly, the FLT is highly sensitive to the microenvironment and can be used as a direct identifier for disorder in cancer cells.

Our main goal was to develop a robust photocatalyst that uses PCET for depleting NADH under biological conditions. To prove the concept, we triggered NADH depletion with fluorenone derivatives (**FL*n***), which can be activated by blue light irradiation with an LED (λ = 456 nm, 24 W). Indeed, we observed that NADH was oxidized to NAD^+ only in the presence of **FL5** (Scheme 2). For the quantification of this transformation, we employed ^{1}H NMR and observed that some of the peaks (such as chemical shift between 8.8 and 8.2 ppm) were slightly shifted due to interactions in the mixtures (Scheme 2). Our initial investigations revealed a turnover number (TON) of 20.6 in the presence of the photocatalyst **FL5** (Table S1, entry 1). To verify the role of the two carboxylic acid groups in **FL5**, we carried out further investigations with different photocatalysts that had either one or no carboxylic acid group (**FL1−4**, entries 2−5, Table S1). We observed lower TONs in the presence of the photocatalysts **FL1−4**, which clearly indicated the importance of the two carboxylic acid groups under the biological conditions.

Scheme 2. ^{1}H NMR of NADH, NAD^+, and Model Photocatalytic Reaction with Irradiation of Light

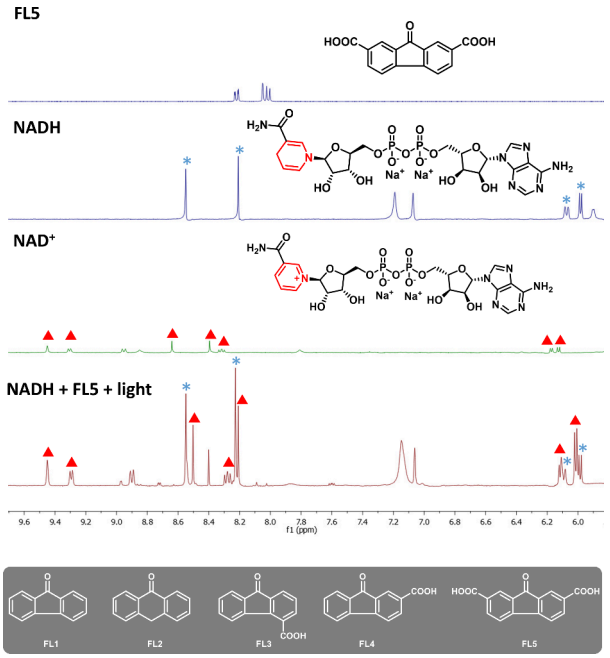

To further increase the TON, we reduced the photocatalyst loading. This increased the TON to 51 (entry 6, Table S1). By decreasing the reaction time, and varying additives, solvent system, and light sources (entries 7−10), we could increase the TON further to 56.6 within 3 h! To clarify the importance of light, photocatalyst, and O_2 in this reaction, we performed control experiments that indicated that the presence of all these parameters was essential for this transformation (entries 12−14).

To further investigate the depletion of NADH under hypoxia, we investigated our optimized catalytic conditions in the absence of O_2, but with cytochrome c (cyt c) as the main oxidant. Generally, cyt c is a small heme protein, which plays the major role in cell apoptosis.[38] It is loosely associated with the inner membrane of the mitochondrion and participates in redox reactions via the transformation of its Fe− center between Fe(II) and Fe(III), which makes it an important component in mitochondrial ETC. We thus considered cyt c as the terminal electron acceptor under hypoxia for the oxidation of NADH in the presence of **FL5** and monitored this with UV−vis spectroscopy (Scheme 3). As it occurs, the absorption peaks at 420, 520, and 550 nm increase in time, clearly indicating the reduction of cyt c(Fe^{III}).[38] In addition, the conversion of NADH to NAD^+ could be monitored by the increasing and decreasing absorption peaks in the range from 250 to 370 nm (more details in Figure S3). It is worth noting that the linear behavior of absorption of the band 550 nm in time could be attributed to the similar reduction rate within 1 h.

Encouraged by the reactivity of our photocatalyst, we investigated the extent of **FL5**'s photocytotoxicity in human breast adenocarcinoma cells (MCF7). For this purpose, cells were treated with 200 μM **FL5** and irradiated with blue laser

https://doi.org/10.1021/jacsau.4c00815
JACS Au 2024, 4, 4856−4865

Scheme 3. Photocatalytic Oxidation of NADH with FL5 and cyt c under Hypoxia

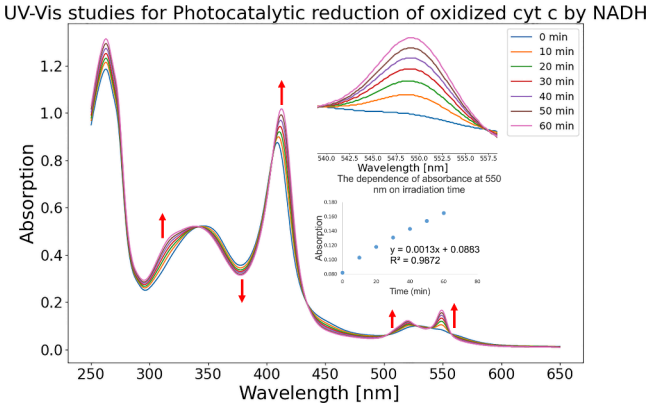

light (λ_{rad} = 460−480 nm) for 60 min. To visualize the cytotoxic effect of **FL5**, we employed FLIM to image mitochondria labeled with the fluorescent probe tetramethyl rhodamine methyl ester (TMRM, $\lambda_{exc/emi}$ = 548/574 nm). This dye is routinely exploited for detecting changes in mitochondrial membrane potential (MMP).[53] In fact, the TMRM is the preferred fluorophore for quantitative MMP measurements because it does not aggregate in cell membranes and shows minimal interaction with membrane proteins. Thus, the trans-mitochondrial membrane distribution of TMRM directly correlates with the membrane potential following Nernst equation.[54] MMP is critical for maintaining the physiological function of ETC to generate ATP. A significant loss of MMP renders cells depleted of energy, leading to subsequent cell death. Usually, one monitors the TMRM fluorescence intensity for quantifying variations in MMP.[55] However, intensity-based measurements are often prone to concentration-dependent artifacts. As an alternative, FLIM is concentration-independent and robust against intensity-based artifacts. Recent work has shown that autofluorescence-based NADH/NADPH FLIM[56] and TMRM-FLIM can discriminate metabolically different cells based on MMP.[53] Furthermore, it has also been demonstrated that the excited-state fluorescence lifetime of TMRM in human colorectal carcinoma cells (HCT116) decreases upon gradual loss of MMP after treatment with the mitochondrial uncoupling agent, trifluoromethoxy carbonylcyanide phenylhydrazone (FCCP).[53] Accordingly, we used FLIM for imaging TMRM-stained mitochondria on **FL5**-treated and blue-light-irradiated MCF7 cells using a custom-built confocal microscope equipped with fast-timing electronics. In particular, we acquired FLIM data sets at three different time points, under "dark" conditions (with **FL5** but no blue light irradiation), after 30 min, and after 60 min of blue light irradiation. We determined fluorescence lifetimes by tail-fitting measured time-correlated single photon counting (TCSPC) histograms with a multiexponential decay model. FLIM imaging was performed in triplicates for each condition examined, and representative images are demonstrated in Scheme 4. Scheme 4A,B shows corresponding average fluorescence lifetime values and fluorescence intensities, respectively, for a representative set of MCF7 cells. In Scheme 4C, fluorescence lifetime values of TMRM from one representative cell (marked with a white circle) for each of the imaging conditions are plotted. We observed a reduction in average fluorescence lifetime from 2.3 ns under "dark" to 1.5 ns after 30 min of blue light exposure. Beyond that, the average

Scheme 4. FLIM Imaging of MCF7 Cells Treated with FL5[a]

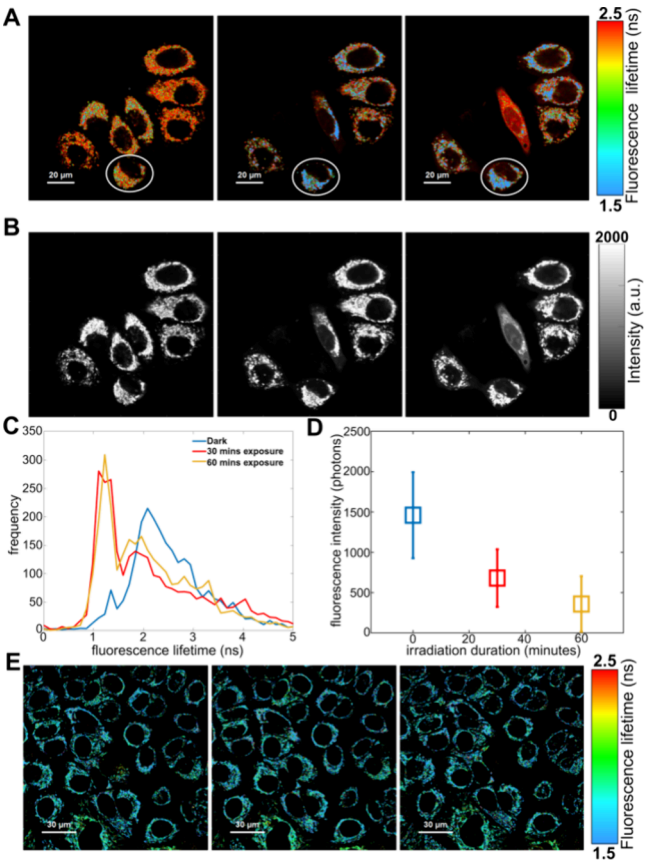

[a]A. FLIM images of MCF7 cells treated with 200 μM of FL5 and stained with TMRM. Left panel shows cells stained and treated with FL5 but no irradiation. Middle and right panels depict the same cells after 30 and 60 min of irradiation, respectively. B. Fluorescence intensity images of same cells as in panel A. C. Comparative plot of fluorescence lifetime values of TMRM in a representative cell under dark (left), after 30 min of photoirradiation (middle), and after 60 min of photoirradiation (right) FLIM images of MCF7 cells stained with TMRM for two sets of control experiments. D. Comparison of fluorescence intensity (photons) recorded from the full image ROIs in panel B. It manifests a drastic drop after 30 min of blue light irradiation and drops further after 60 min of exposure. E. Cells were not treated with FL5 and imaged under dark (left panel), irradiated for 30 (middle panel), and 60 min (right panel).

lifetime after irradiation remains constant at 1.5 ns even after 60 min of irradiation, which strongly indicates that blue light irradiation for the initial 30 min was sufficient for the photoactivation of **FL5**. However, the presence of a second cell in the same ROI (Scheme 4A) exhibits an increase in average FLT (fluorescence lifetime). As demonstrated earlier for HCT116 cells treated with FCCP,[53] depolarization of MMP is manifested by an increase in TMRM FLT. Therefore, to avoid any ambiguous inference from our FLIM data, we decided to compare fluorescence intensities instead. As illustrated in Scheme 4D, when we compared the fluorescence intensity (photons) recorded from the full image ROI, it manifests a drastic drop after 30 min of blue light irradiation and drops further after 60 min of exposure. It is well-known that in case of loss of MMP, TMRM is dispersed throughout the cell cytosol and fluorescence signal at mitochondria drop dramatically. Loss of MMP indicates bioenergetic and metabolic stress and might result in the release of apoptotic factors leading to cell death. To

https://doi.org/10.1021/jacsau.4c00815
JACS Au 2024, 4, 4856−4865

validate our findings further, two independent sets of control measurements were also performed. In the first set, we did not treat cells with **FL5** (Scheme 4E). In the second set, cells were treated with **FL5** but without blue light irradiation (FigureS4 in the Supporting Information). To our delight, we did not observe any obvious change in fluorescence lifetime up to 60 min, which clearly confirmed that both the presence of photocatalyst and light are essential. Furthermore, we also conducted TMRM-FLIM experiments on MCF7 cells treated with **FL1** and **FL4** (Figures S5 and S6) and did not observe obvious changes in FLT values.

Inspired by the results of our FLIM experiments, we performed CellROX assays on MCF7 cells to confirm whether the photoactivated photocatalyst (**FL5**) led to any intracellular oxidative stress and generation of ROS species.[57,58] In a CellROX assay, a cell-permeant fluorogenic probe (CellROX Orange Reagent) is utilized for measuring the oxidative stress in living cells. It relies on the membrane-permeable dye CellROX Orange Reagent, which is nonfluorescent in its reduced state but exhibits bright orange fluorescence when oxidized by ROS, with the maximum absorption/emission wavelengths of ∼545/565 nm. To investigate this, MCF7 cells were treated with 5 μM CellROX and were irradiated with blue laser light in the presence of 200 μM of **FL5**. In fact, after irradiation for 30 min, we observed an increased brightness and global increase in fluorescence intensity of these cells (Scheme 5B) as compared to

Scheme 5. CellROX Assay on MCF7 Cells[a]

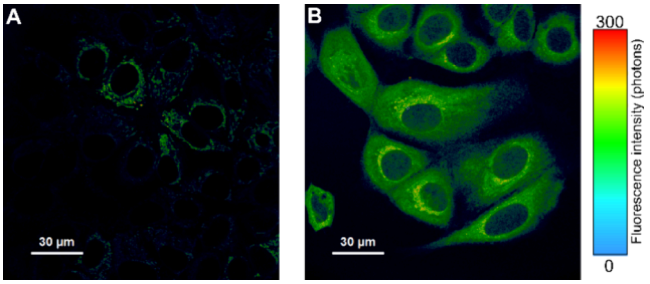

[a]A. Confocal micrographs of a set of MCF7 cells reacted with 5 μM of CellROX. Only autofluorescence is visible. B. Cells treated with **FL5** and exposed to blue light for 30 min manifesting a strong increase in fluorescence signal.

the control (without **FL5** treatment irradiation) (Scheme 5A). Since ROS serves as the main oxidizing agent of CellROX to generate a fluorescent product, the observed strong increase in fluorescence of CellROX orange affirms the buildup of intracellular ROS under normoxia upon **FL5** treatment and photoirradiation (CellROX is known to detect O_2^- and •OH). For further proving the formation of H_2O_2, photogenerated H_2O_2 was detected and analyzed in the presence of triphenylphosphine (PPh_3) by GC-MS (see Figure S2 in the Supporting Information).

Next, we investigated the effect of **FL5** treatment and photoirradiation on hypodermal mitochondria of the live nematode *C. elegans*. For this purpose, we took advantage of worms that bear mutation within the src-1 gene, an orthologue of several human proto-oncogenes. [//wormbase.org]. The src-1 mutant worms were cultured on an NGM agar plate containing 100 nM TMRM for 2 days in the dark to ensure strong staining of hypodermal mitochondria. Then, worms were treated with 200 μM of **FL5** on NGM plates, placed for microscopy on an agar pad in 500 μM of **FL5**, and irradiated with blue light (λ_{rad} = 460−480 nm) for 30 min. FLIM imaging was performed using a custom-built confocal microscope, as described before for MCF7 cells. In case of **FL5**-treated and photoirradiated hypodermis sections, we obtained a shift in mean fluorescence lifetime value of TMRM from 2.7 ns under "dark" to 2.1 ns after 30 min of blue light exposure (Scheme 6A,B). Most importantly,

Scheme 6. FLIM Images of TMRM-Stained Mitochondria in Hypodermis of a Live FL5-Treated *C. elegans*[a]

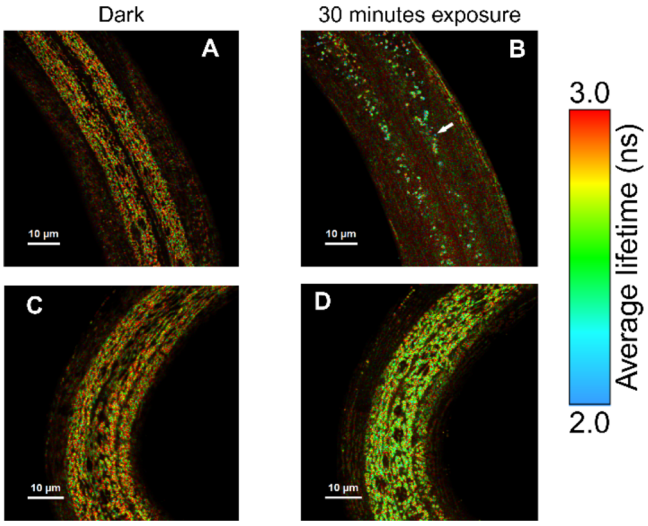

[a]A. An **FL5**-treated worm, tubular mitochondrial organization before irradiation under dark conditions. B. Reorganization of tubular structures of mitochondria into vesicular spheroids due to oxidative stress after irradiation for 30 min in the same worm. C. No treatment with **FL5**, FLIM image under dark conditions shows healthy tubular mitochondria. D. After irradiation for 30 min, morphology of mitochondria remains as before.

we also observe that photoactivation of FL5 upon blue light exposure for 30 min resulted in a drastic reorganization of mitochondrial morphology in the worm's hypodermis from tubule-like (Scheme 6A) to vesicle-like and led to the loss of TMRM-stained functional mitochondria with intact membrane potential (Scheme 6B). Interestingly, a similar transition of the mitochondrial structure from tubular to donut or blob shape was previously observed in cells upon oxidative stress.[59] In this previous study, calcium uptake in mitochondria was found to be an important mediator in the mitochondrial shape transition. Furthermore, it was also demonstrated that generation of mitochondrial ROS led to a change in shape from tubular to donut or blob shapes. Mitochondrial organization in hypodermis of non-**FL5**-treated worms was similar before and after irradiation (Scheme 6C,D). These sets of experiments confirm, first, that **FL5** freely permeates into the hypodermis of intact worms. Second, transition of mitochondrial shape and the loss of intact mitochondria (hence, MMP) stronglyindicates bioenergetics and metabolic stress as that correlates with our previous observations on MCF7 cells.

To further examine the photocytotoxicity of **FL5**, a viability assay of MCF7 with **FL5** was carried out as described earlier (Scheme 7).[60,61] MCF7 cells were stained with a viability marker (Acridin/Propidium iodide (PI) logos #F23001) and counted with an automated fluorescence cell counter LUNA FX7 (https://logosbio.com/luna-fx7/) to determine the ratio

https://doi.org/10.1021/jacsau.4c00815
JACS Au 2024, 4, 4856−4865

Scheme 7. Viability Assay of MCF7 Cells Treated with FL5[a]

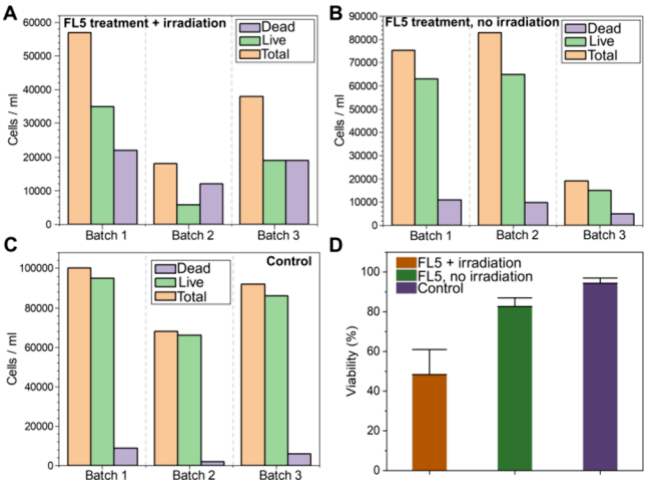

[a]A. Bar plots showing cells/mL counted after **FL5** treatment and blue light irradiation for 120 min. A significant number of dead cells are observed for each batch. B. Counting results for cells treated with **FL5** but without irradiation. C. Cells that received no treatment with **FL5** and no irradiation were done. D. Comparison of viability percentages from counted cells in three batches shows a substantial drop in cell viability in case of cells with photoactivated **FL5**.

between live and dead cells. In particular, cells were seeded in 3.5 cm ibidi glass-bottom dishes (ibidi no. 81158; for details on cell culture, see Supporting Information). At first, we conducted a viability assay on MCF7 cells treated with 0, 50, 100, 200, 400, and 800 μM of **FL5** followed by blue light irradiation for 2 h (Figure S7). These cell counting experiments confirm that for 200 μM **FL5** treated cells, the viability drops to ∼50%, indicating the half-maximal inhibitory concentration (IC50) dose. Hence, we continued further investigations using 200 μM of **FL5**. For quantifying the number of live and dead cells, cells were first treated with 200 μM of **FL5** and irradiated with blue light for 2 h; second, cells were treated with 200 μM of **FL5** but not irradiated; and finally, cells were neither treated with **FL5** nor irradiated. In contrast to our FLIM measurements, we now increased the duration of photoirradiation from 60 to 120 min. This was done because, although a minimum of 30 min irradiation was enough to induce oxidative stress as seen by the reduction in TMRM fluorescence, it was not enough to induce cell death. Hence, cells were monitored after blue light irradiation for 60, 90, and 120 min, and we found that a minimum irradiation time of 120 min is required to induce cell death. Furthermore, we also checked the phototoxicity of blue light irradiation in the absence of **FL5** and ruled out any possible cytotoxic effects of irradiation alone. Scheme 7 presents the results of cell counting assays for MCF7 cells from three different passages in three different days (noted as batches 1, 2, and 3). Scheme 7A–C shows bar histograms depicting the number of dead cells/mL (purple), number of live cells/mL (green), and total number of cells/mL (orange) for each of the batches. For all batches, a substantial increase in the number of dead cells (∼39%) was observed after treatment with **FL5** followed by irradiation (Scheme 7A). In contrast, we observed an insignificant reduction of the number of live cells for **FL5**-treated that were not exposed to blue light (Scheme 7B), similar to the "no treatment" control batch (∼6%) (Scheme 7C). These findings confirmed that photoactivated **FL5** was indeed capable of inducing cell death in tumor cells. Finally, yet importantly, we compared the fraction of viable MCF7 cells under different conditions. As shown in Scheme 7D, cells, which received **FL5** treatment and irradiation, showed a significant drop in viability to 52 ± 8% (dark orange), from an initial viability of 93 ± 5% (violet) for the no-treatment controls. For MCF7 cells that received **FL5** treatment but no irradiation, a minor drop in viability to 85 ± 4% was observed (green bar, Scheme 7D). The mean values and standard deviations of cell viability were calculated by dividing the number of live cells by the total number of cells using cell counting data from three batches (batches 1–3, Scheme 7).

To further corroborate the experimental findings, density functional theory calculations for different photocatalysts were performed (**FL1**, **FL4**, and **FL5** in Scheme 8).[62] The reaction

Scheme 8. Free Energy Profiles of the Oxidation of NADH Catalyzed by FL*n* under Normoxia

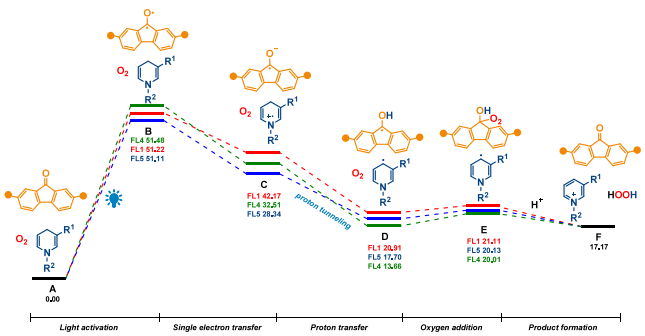

The unit of all energies is kcal/mol.

started with light absorption of chromophore **FL*n*** (**A**), which resulted in its excitation to the singlet excited state that decayed into a long-lived triplet state (**B**). Here, we considered that the reactions take place on the triplet potential energy surface. The reaction proceeds with NADH approaching photocatalyst **FL*n*** in its lowest triplet state, and a single electron transfer occurs from NADH to **FL*n***, forming a charge-transfer complex (**C**). A spin density plot (Figure S8A) shows that, indeed, **FL*n*$^-$** and NADH$^+$ were formed. In an almost barrierless way, thus almost simultaneously, a proton was transferred to form the NAD and **FL*n*** radicals (**D**). Thus, this process resembles a proton-coupled electron transfer. The NAD radical can react further, and the photocatalyst (**FL*n***) can regenerate by oxidation with O_2, first forming an **FL*n*-O_2** complex (**E**) and, subsequently, by elimination of •OOH, forming a van der Waals complex, leading to the return of **FL*n*** to its ground state (**F**). Ultimately, H_2O_2 is formed.

The reaction without a photocatalyst (NADH + O_2 → NAD• + HOO•) has a ΔE_r of 20.54 kcal/mol (ΔG_r^{298} = 17.17 kcal/mol) and an activation energy of ΔE_a of 18.21 kcal/mol (ΔG_r^{298} = 23.23 kcal/mol). After the TS, a van der Waals complex is formed that lies 11.62 kcal/mol (ΔG^{298} = 18.09 kcal/mol) above the energy level of the reactants. This hydrogen atom transfer is endothermic and does not proceed easily. The photocatalyst clearly facilitates this step by allowing electron and proton transfer to occur almost simultaneously. This implies that the tunneling probability of the proton has also to be taken into account.[62]

The reaction and activation energies for the photocatalyzed steps are summarized in Table S3, together with the electron affinities and excitation energy of the lowest triplet state for **FL*n***.

https://doi.org/10.1021/jacsau.4c00815
JACS Au 2024, 4, 4856–4865

The overall reaction energetics is (obviously) the same as for the noncatalyzed reaction. However, after initial photoexcitation to the triplet state of **FL*n***, the reaction is downhill. The excitation toward ^{3}**FL*n*** is the same for all three considered compounds. However, a large difference is found in the SET step from B to C: for **FL1**, it is exothermic by 23.23 kcal/mol (ΔG^{298} = −9.05 kcal/mol), while for **FL5**, this step is much more exothermic, ΔE = −37.18 kcal/mol (ΔG^{298} = −22.77 kcal/mol). This significant difference is caused by the higher electron affinity (EA) of **FL5** compared to **FL1**, which is already the case for the ground state, and is even more enhanced in the triplet state due to the presence of the electron withdrawing carboxylic groups. Figure S8B shows the spin density calculated for **FL5**$^-$. The negative charge on **FL5** is delocalized also over the COOH groups, which stabilizes the negative charge even more. The calculations indicate that the higher activity of **FL5** over **FL1** can be linked to the significantly higher electron affinity of **FL5** in its triplet state. The −COOH groups stabilize the anion by delocalization of the negative charge. Other substituents that can stabilize a negative charge are also expected to result in higher activity.

Furthermore, for examining the steady-state photoluminescence (PL) (Scheme 9A) of **FL1**, **FL4**, and **FL5**, 10 mg of photocatalyst were completely dissolved in 1 mL of DMSO. The PL emission maximum of **FL1** is at 518 nm, **FL4** is at 505 nm, and **FL5** is at 491 nm. To understand charge carrier generation and recombination, we measured the PL decays of **FL1**, **FL4**, and **FL5** at their respective emission wavelengths (Scheme 9B). For all samples, the PL decay profiles were recorded with TCSPC and fitted with a biexponential decay function. Average PL lifetimes are 13.67 ± 0.01 ns for **FL1**, 4.98 ± 0.01 ns for **FL4**, and 1.57 ± 0.02 ns for **FL5**. These lifetimes were found to decrease substantially from **FL1** to **FL5** upon addition of carboxylic acid groups, as can be seen from the fit parameters in Table S2. Especially, the long-lifetime recombination (τ_2) decreased from 13.70 ns (**FL1**) to 2.96 ns (**FL5**), along with an increase of the amplitude of the fast recombination component (A1), from 17% in **FL1** to 92% in **FL5**. Such a significant difference suggests that apart from the radiative and nonradiative recombination, another major factor affects the carrier recombination dynamics. For confirmation, we also calculated the rate of electron transfer in **FL5**, where two carboxylic acid functional groups are present, and in **FL4**, where one carboxylic acid functional group is present. The rate of electron transfer in **FL5** was found to have a larger effect than for **FL4** (more details in Supporting Information). These results confirm that the incorporation of carboxylic groups promotes efficient proton tunneling and the higher electron affinity of **FL5**.

Scheme 9. Photoluminescence Studies of the Photocatalysts[a]

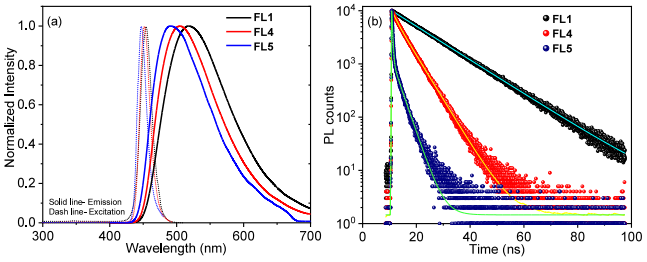

[a](a) Excitation and emission spectra, and (b) lifetime profiles of solutions of organic dyes in DMSO.

Combining the results of our experimental investigations with DFT calculations, we propose the mechanisms shown in Scheme 10 for the photocatalytic oxidation of NADH under normoxia and hypoxia. Under normoxia, the photocatalyst is activated by blue light and reductively quenched by NADH (**I**) via an electron transfer (ET) proton transfer (PT) process, resulting in the formation of NAD• (**II**). Oxygen (**IV**) is the key electron acceptor to regenerate the photocatalyst and form the resulting radical **V**. **II** is further oxidized by **V** to provide NAD$^+$ (**III**) and H_2O_2 (**VI**), which was probed with the measurements of oxidative stress. Under hypoxia, cyt c (Fe^{III}) (**VII**) was used as an electron acceptor instead of O_2 and resulted in the photocatalytic depletion of NADH under hypoxia.

Scheme 10. Proposed Mechanisms for Photocatalytic Oxidation of NADH under Normoxia and Hypoxia

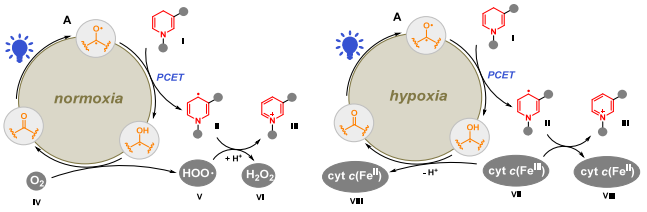

In summary, a PCET process has been developed that leads to the efficient depletion of NADH and disruption of the electron transport chain (ETC). A functionalized photocatalyst with two carboxylic acid groups exhibited an enhanced oxidation ability and stabilized the intermediates during electron transfer. Furthermore, the presence of carboxylic acid groups improved the solubility of the photocatalyst, facilitating the electron transfer inside tissues or in cancer cells.[63] Our experimental studies and detailed mechanistic analyses contribute to a comprehensive understanding of the redox processes connected with PCET and the modulation of the triplet excited state. We believe that this study will spur the development of more effective strategies for photodynamic therapy.

ASSOCIATED CONTENT

Supporting Information

The Supporting Information is available free of charge at https://pubs.acs.org/doi/10.1021/jacsau.4c00815.

Optimization of reactions, GC-MS analysis, cell culture, viability assay, mitochondria staining, preparation of the *C. elegans* sample, FLIM data, evaluation of fluorescence lifetime data, steady-state photoluminescence (PL) analysis, and detail of theoretical calculations (PDF)

AUTHOR INFORMATION

Corresponding Authors

Jörg Enderlein − *Third Institute of Physics - Biophysics, Georg-August-Universität Göttingen, Göttingen 37077, Germany;* orcid.org/0000-0001-5091-7157; Email: joerg.enderlein@phys.uni-goettingen.de

Shoubhik Das − *Department of Chemistry, University of Antwerp, Antwerp 2020, Belgium; Department of Chemistry, University of Bayreuth, Bayreuth 95447, Germany;* orcid.org/0000-0002-4577-438X; Email: shoubhik.das@uni-bayreuth.de

https://doi.org/10.1021/jacsau.4c00815
JACS Au 2024, 4, 4856−4865

Authors

Tong Zhang − *Department of Chemistry, University of Antwerp, Antwerp 2020, Belgium*

Arindam Ghosh − *Third Institute of Physics - Biophysics, Georg-August-Universität Göttingen, Göttingen 37077, Germany; Department of Biotechnology and Biophysics, University of Würzburg, Würzburg 97074, Germany;* orcid.org/0000-0002-5712-1271

Lisa Behringer-Pließ − *Department of Biotechnology and Biophysics, University of Würzburg, Würzburg 97074, Germany*

Lata Chouhan − *Department of Chemistry, KU Leuven, Leuven 3001, Belgium;* orcid.org/0000-0002-2484-9338

Ana V. Cunha − *Department of Chemistry, University of Antwerp, Antwerp 2020, Belgium;* orcid.org/0000-0001-8996-2860

Remco W. A. Havenith − *Stratingh Institute for Chemistry and Zernike Institute for Advanced Materials, University of Groningen, Groningen, AG 9747, The Netherlands; Ghent Quantum Chemistry Group, Department of Chemistry, Ghent University, Gent 9000, Belgium;* orcid.org/0000-0003-0038-6030

Eugenia Butkevich − *Third Institute of Physics - Biophysics, Georg-August-Universität Göttingen, Göttingen 37077, Germany*

Lei Zhang − *Department of Chemistry & Center for Synthetic Microbiology (SYNMIKRO), Philipps-Universität Marburg, Marburg 35032, Germany*

Olalla Vázquez − *Department of Chemistry & Center for Synthetic Microbiology (SYNMIKRO), Philipps-Universität Marburg, Marburg 35032, Germany;* orcid.org/0000-0002-7555-1865

Elke Debroye − *Department of Chemistry, KU Leuven, Leuven 3001, Belgium;* orcid.org/0000-0003-1087-4759

Complete contact information is available at: https://pubs.acs.org/10.1021/jacsau.4c00815

Author Contributions

‡T.Z. and A.G. contributed equally. The manuscript was written through contributions of all authors. All authors have given approval to the final version of the manuscript.

Notes

The authors declare no competing financial interest.

■ ACKNOWLEDGMENTS

S.D. thanks the Francqui start up grant from the University of Antwerp, Belgium, for the financial support. T.Z. thanks FWO SB PhD fellowship for their financial assistance to finish this work. A.G. thanks Markus Sauer for generous provision of resources to perform cell viability assays. J.E. is grateful for financial support by the Deutsche Forschungsgemeinschaft (DFG, German Research Foundation) under Germany's Excellence Strategy-EXC 2067/1-390729940, and he thanks the European Research Council (ERC) for financial support via project "smMIET" (grant agreement no. 884488) under the European Union's Horizon 2020 research and innovation program. R.W.A.H. was sponsored by NWO Exact and Natural Sciences for the use of supercomputer facilities (contract nr. 17197 7095). R.W.A.H. and A.V.C. thank S. Dolas (SURF, NL) for allowing us to perform calculations on the experimental AMD platform kleurplaat maintained and operated by SURF Open Innovation Lab.

■ REFERENCES

(1) Parada, G. A.; Goldsmith, Z. K.; Kolmar, S.; Rimgard, B.; Mercado, B. Q.; Hammarström, L.; Hammes-Schiffer, S.; Mayer, J. M. Concerted proton−electron transfer reactions in the Marcus inverted region. *Science* **2019**, *364*, 471−475.

(2) Zhou, Z.; Chen, Z.; Kang, X.-W.; Zhou, Y.; Wang, B.; Tang, S.; Zou, S.; Zhang, Y.; Hu, Q.; Bai, F.; Ding, B.; Zhong, D. The nature of proton−coupled electron transfer in a blue light using flavin domain. *Proc. Natl. Acad. Sci. U. S. A.* **2022**, *119*, No. e2203996119.

(3) Schneider, J.; Bangle, R. E.; Swords, W. B.; Troian-Gautier, L.; Meyer, G. J. Determination of Proton−Coupled Electron Transfer Reorganization Energies with Application to Water Oxidation Catalysts. *J. Am. Chem. Soc.* **2019**, *141*, 9758−9763.

(4) Tyburski, R.; Liu, T. S.; Glover, D.; Hammarstrom, L. Proton−Coupled Electron Transfer Guidelines, Fair and Square. *J. Am. Chem. Soc.* **2021**, *143*, 560−576.

(5) Mayer, J. M. Proton−Coupled Electron Transfer: A Reaction Chemist's View. *Annu. Rev. Phys. Chem.* **2004**, *55*, 363−390.

(6) Huynh, M. H. V.; Meyer, T. J. Proton−Coupled Electron Transfer. *Chem. Rev.* **2007**, *107*, 5004−5064.

(7) Reece, S. Y.; Hodgkiss, J. M.; Stubbe, J.; Nocera, D. G. Proton−coupled electron transfer: the mechanistic underpinning for radical transport and catalysis in biology. *Philos. Trans. R. Soc. B* **2006**, *361*, 1351−1364.

(8) Kojima, T. Study on Proton−Coupled Electron Transfer in Transition Metal Complexes. *Bull. Chem. Soc. Jpn.* **2020**, *93*, 1571−1582.

(9) Liu, T.; Guo, M.; Orthaber, A.; Lomoth, R.; Lundberg, M.; Ott, S.; Hammarström, L. Accelerating proton−coupled electron transfer of metal hydrides in catalyst model reactions. *Nature Chem.* **2018**, *10*, 881−887.

(10) Masgrau, L.; Roujeinikova, A.; Johannissen, L. O.; Hothi, P.; Basran, J.; Ranaghan, K. E.; Mulholland, A. J.; Sutcliffe, M. J.; Scrutton, N. S.; Leys, D. Atomic Description of an Enzyme Reaction Dominated by Proton Tunneling. *Science* **2006**, *312*, 237−241.

(11) Wenger, O. S. Proton−Coupled Electron Transfer with Photoexcited Metal Complexes. *Acc. Chem. Res.* **2013**, *46*, 1517−1526.

(12) Usharani, D.; Lacy, D. C.; Borovik, A. S.; Shaik, S. Dichotomous Hydrogen Atom Transfer vs Proton−Coupled Electron Transfer During Activation of X−H Bonds (X = C, N, O) by Nonheme Iron−Oxo Complexes of Variable Basicity. *J. Am. Chem. Soc.* **2013**, *135*, 17090−17104.

(13) Klein, J. E. M. N.; Knizia, G. cPCET versus HAT: A Direct Theoretical Method for Distinguishing X−H Bond−Activation Mechanisms. *Angew. Chem., Int. Ed.* **2018**, *57*, 11913−11917.

(14) Capaldo, L.; Ravelli, D.; Fagnoni, M. Direct Photocatalyzed Hydrogen Atom Transfer (HAT) for Aliphatic C−H Bonds Elaboration. *Chem. Rev.* **2022**, *122*, 1875−1924.

(15) Cao, H.; Tang, X.; Tang, H.; Yuan, Y.; Wu, J. Photoinduced intermolecular hydrogen atom transfer reactions inorganic synthesis. *Chem. Catalysis* **2021**, *1*, 523−598.

(16) Migliore, A.; Polizzi, N. F.; Therien, M. J.; Beratan, D. N. Biochemistry and Theory of Proton−Coupled Electron Transfer. *Chem. Rev.* **2014**, *114*, 3381−3465.

(17) Miller, D. C.; Tarantino, K. T.; Knowles, R. R. Proton−Coupled Electron Transfer in Organic Synthesis: Fundamentals, Applications, and Opportunities. *Top. Curr. Chem.* **2016**, *374*, 30.

(18) Cavin, S.; Gkasti, A.; Faget, J.; Hao, Y.; Letovanec, I.; Reichenbach, M.; Gonzalez, M.; Krueger, T.; Dyson, P. J.; Meylan, E.; Perentesa, J. Y. Low−dose photodynamic therapy promotes a cytotoxic immunological response in a murine model of pleural mesothelioma. *Eur. J. Cardiothorac. Surg.* **2020**, *58*, 783−791.

(19) Bevernaegie, R.; Doix, B.; Bastien, E.; Diman, A.; Decottignies, A.; Feron, O.; Elias, B. Exploring the Phototoxicity of Hypoxic Active Iridium(III)−Based Sensitizers in 3D Tumor Spheroids. *J. Am. Chem. Soc.* **2019**, *141*, 18486−18491.

(20) Peng, J.; Du, K.; Sun, J.; Yang, X.; Wang, X.; Zhang, X.; Song, G.; Feng, F. Photocatalytic Generation of Hydrogen Radical (H·) with GSH for Photodynamic Therapy. *Angew. Chem., Int. Ed.* **2023**, *62*, No. e202214991.
(21) Yu, F.; Shao, Y.; Chai, X.; Zhao, Y.; Li, L. Spatially Selective Monitoring of Subcellular Enzyme Dynamics in Response to Mitochondria-Targeted Photodynamic Therapy. *Angew. Chem., Int. Ed.* **2022**, *61*, No. e202203238.
(22) Yuan, J.; Zhou, Q.-H.; Xu, S.; Zuo, Q.-P.; Li, W.; Zhang, X.-X.; Ren, T.-B.; Yuan, L.; Zhang, X.-B. Enhancing the Release Efficiency of a Molecular Chemotherapeutic Prodrug by Photodynamic Therapy. *Angew. Chem., Int. Ed.* **2022**, *61*, No. e202206169.
(23) Bergmann, L.; Hedley, G. J.; Baumann, T.; Bräse, S.; Samuel, I. D. W. Direct observation of intersystem crossing in a thermally activated delayed fluorescence copper complex in the solid state. *Sci. Adv.* **2016**, *2*, No. e1500889.
(24) Hu, D.; Yao, L.; Yang, B.; Ma, Y. Reverse intersystem crossing from upper triplet levels to excited singlet: a 'hot excition' path for organic light−emitting diodes. *Philos. Trans. R. Soc. A* **2015**, *373*, 20140318.
(25) Zobel, J. P.; Wernbacher, A. M.; González, L. Efficient Reverse Intersystem Crossing in Carbene−Copper−Amide TADF Emitters via an Intermediate Triplet State. *Angew. Chem., Int. Ed.* **2023**, *62*, No. e202217620.
(26) Dolmans, D. E.; Fukumura, D.; Jain, R. K. Photodynamic therapy for cancer. *Nat. Rev. Cancer.* **2003**, *3*, 380−387.
(27) Henderson, B. W.; Dougherty, T. J. How does photodynamic therapy work? *Photochem. Photobiol.* **1992**, *55*, 145−157.
(28) Chen, F.; Huang, H.; Guo, L.; Zhang, Y.; Ma, T. The Role of Polarization in Photocatalysis. *Angew. Chem., Int. Ed.* **2019**, *58*, 10061−10073.
(29) Teng, K.-X.; Niu, L.-Y.; Yang, Q.-Z. Supramolecular Photosensitizer Enables Oxygen−Independent Generation of Hydroxyl Radicals for Photodynamic Therapy. *J. Am. Chem. Soc.* **2023**, *145*, 4081−4087.
(30) Chu, J. C. H.; Wong, C. T. T.; Ng, D. K. P. Toward Precise Antitumoral Photodynamic Therapy Using a Dual Receptor-Mediated Bioorthogonal Activation Approach. *Angew. Chem., Int. Ed.* **2023**, *62*, No. e202214473.
(31) Zhao, J.; Yang, Y.; Xu, X.; Li, H.; Fei, J.; Liu, Y.; Zhang, X.; Li, J. Super Light−Sensitive Photosensitizer Nanoparticles for Improved Photodynamic Therapy against Solid Tumors. *Angew. Chem., Int. Ed.* **2022**, *61*, No. e202210920.
(32) Barsoum, I. B.; Smallwood, C. A.; Siemens, D. R.; Graham, C. H. A mechanism of hypoxia−mediated escape from adaptive immunity in cancer cells. *Cancer Res.* **2014**, *74*, 665−674.
(33) Sun, Q.; Su, Q.; Gao, Y.; Zhou, K.; Song, W.; Quan, P.; Yang, X.; Ge, Z.; Zhang, Y.; He, G. Cationic telluroviologen derivatives as type-I photosensitizers for tumor photodynamic theranostics. *Aggregate* **2023**, *4*, No. e298.
(34) Xu, C.; Zou, H.; Zhao, Z.; Zhang, P.; Kwok, R. T. K.; Lam, J. W. Y.; Sung, H. H. Y.; Williams, I. D.; Tang, B. Z. A New Strategy toward "Simple" Water-Soluble AIE Probes for Hypoxia Detection. *Adv. Funct. Mater.* **2019**, *29*, No. 1903278.
(35) Wang, L.; Hu, R.; Qin, A.; Tang, B. Z. Conjugated Polymers with Aggregation-Induced Emission Characteristics for Fluorescence Imaging and Photodynamic Therapy. *ChemMedChem.* **2021**, *16*, 2330−2338.
(36) Pagliaricci, N.; Pettinari, R.; Marchetti, F.; Pettinari, C.; Cappellacci, L.; Tombesi, A.; Cuccioloni, M.; Hadijid, M.; Dyson, P. J. Potent and Selective Anticancer Activity of Half−sandwich Ruthenium and Osmium Complexes with Modified Curcuminoid Ligands. *Dalton Trans.* **2022**, *51*, 13311−13321.
(37) Schoch, S.; Hadiji, M.; Pereira, S. A. P.; Saraiva, M. L. M. F. S.; Braccini, S.; Chiellini, F.; Biver, T.; Zacchini, S.; Pampaloni, G.; Dyson, P. J.; Marchetti, F. A Strategy to Conjugate Bioactive Fragments to Cytotoxic Diiron Bis(cyclopentadienyl) Complexes. *Organometallics* **2021**, *40* (15), 2516−2528.
(38) Huang, H.; Banerjee, S.; Qiu, K.; Zhang, P.; Blacque, O.; Malcomson, T.; Paterson, M. J.; Clarkson, G. J.; Staniforth, M.; Stavros, V. G.; Gasser, G.; Chao, H.; Sadler, P. J. Targeted photoredox catalysis in cancer cells. *Nat. Chem.* **2019**, *11*, 1041−1048.
(39) Liu, Z.; Romero-Canelón, I.; Qamar, B.; Hearn, J. M.; Habtemariam, A.; Barry, N. P. E.; Pizarro, A. M.; Clarkson, G. J.; Sadler, P. J. The Potent Oxidant Anticancer Activity of Organoiridium Catalysts. *Angew. Chem.* **2014**, *126*, 4022−4027.
(40) Zhang, P.; Chiu, C. K. C.; Huang, H.; Lam, Y. P. Y.; Habtemariam, A.; Malcomson, T.; Paterson, M. J.; Clarkson, G. J.; O'Connor, P. B.; Chao, H.; Sadler, P. J. Organoiridium Photosensitizers Induce Specific Oxidative Attack on Proteins within Cancer Cells. *Angew. Chem., Int. Ed.* **2017**, *56*, 14898−14902.
(41) Imberti, C.; Zhang, P.; Huang, H.; Sadler, P. J. New Designs for Phototherapeutic Transition Metal Complexes. *Angew. Chem., Int. Ed.* **2020**, *59*, 61−73.
(42) Wendoloski, J. J.; Matthew, J. B.; Weber, P. C.; Salemme, F. R. Molecular Dynamics of a Cytochrome c−Cytochrome b_5 Electron Transfer Complex. *Science* **1987**, *238*, 794−797.
(43) Gamero-Quijano, A.; Bhattacharya, S.; Cazade, P.-A.; Molina-Osorio, A. F.; Beecher, C.; Djeghader, A.; Soulimane, T.; Dossot, M.; Thompson, D.; Herzog, G.; Scanlon, M. D. Modulating the pro−apoptotic activity of cytochrome c at a biomimetic electrified interface. *Sci. Adv.* **2021**, *7*, No. eabg4119.
(44) Kluck, R. M.; Bossy-Wetzel, E.; Green, D. R.; Newmeyer, D. D. The Release of Cytochrome c from Mitochondria: A Primary Site for Bcl−2 Regulation of Apoptosis. *Science* **1997**, *275*, 1132−1136.
(45) Saura, Pa; Kaila, V. R. I. Energetics and Dynamics of Proton−Coupled Electron Transfer in the NADH/FMN Site of Respiratory Complex I. *J. Am. Chem. Soc.* **2019**, *141*, 5710−5719.
(46) Yayla, H. G.; Knowles, R. R. Proton−Coupled Electron Transfer in Organic Synthesis: Novel Homolytic Bond Activations and Catalytic Asymmetric Reactions with Free Radicals. *Synlett* **2014**, *25*, 2819−2826.
(47) Amorati, R.; Valgimigli, L.; Baschieri, A.; Guo, Y.; Mollica, F.; Menichetti, S.; Lupi, M.; Viglianisi, C. SET and HAT/PCET acid−mediated oxidation processes in helical shaped fused bis−phenothiazines. *ChemPhysChem* **2021**, *22*, 1446−145.
(48) da Silva, G. Carboxylic Acid Catalyzed Keto−Enol Tautomerizations in the Gas Phase. *Angew. Chem.* **2010**, *122*, 7685−7687.
(49) Morita, H.; Nagakura, S. O−H overtone bands and potential energy curves of the hydrogen−bonded formic and acetic acids. *J. Mol. Spectrosc.* **1972**, *42*, 536−546.
(50) Lassalas, P.; Gay, B.; Lasfargeas, C.; James, M. J.; Tran, V.; Vijayendran, K. G.; Brunden, K. R.; Kozlowski, M. C.; Thomas, C. J.; Smith, A. B., III; Huryn, D. M.; Ballatore, C. Structure Property Relationships of Carboxylic Acid Isosteres. *J. Med. Chem.* **2016**, *59*, 3183−3203.
(51) Datta, R.; Alfonso-García, A.; Cinco, R.; Gratton, E. Fluorescence lifetime imaging of endogenous biomarker of oxidative stress. *Sci. Rep.* **2015**, *5* (1), No. 9848.
(52) Bastiaens, P. I.; Squire, A. Fluorescence lifetime imaging microscopy: spatial resolution of biochemical processes in the cell. *Trends Cell Biol.* **1999**, *9* (2), 48−52.
(53) Okkelman, I. A.; Papkovsky, D. B.; Dmitriev, R. I. Estimation of the mitochondrial membrane potential using fluorescence lifetime imaging microscopy. *Cytometry Part A* **2020**, *97* (5), 471−482.
(54) Gerencser, A. A.; Chinopoulos, C.; Birket, M. J.; Jastroch, M.; Vitelli, C.; Nicholls, D. G.; Brand, M. D. Quantitative measurement of mitochondrial membrane potential in cultured cells: calcium-induced de-and hyperpolarization of neuronal mitochondria. *J. Physiol.* **2012**, *590* (12), 2845−2871.
(55) Joshi, D. C.; Bakowska, J. C. Determination of mitochondrial membrane potential and reactive oxygen species in live rat cortical neurons. *J. Visualized Exp.* **2011**, *51*, No. e2704.
(56) Blacker, T. S.; Mann, Z. F.; Gale, J. E.; Ziegler, M.; Bain, A. J.; Szabadkai, G.; Duchen, M. R. Separating NADH and NADPH fluorescence in live cells and tissues using FLIM *Nat. Commun.* **2014**, *5*, 3936.

https://doi.org/10.1021/jacsau.4c00815
JACS Au 2024, 4, 4856−4865

(57) Choi, H.; Yang, Z.; Weisshaar, J. C. Single-cell, real-time detection of oxidative stress induced in Escherichia coli by the antimicrobial peptide CM15. *Proc. Natl. Acad. Sci. U. S. A.* **2015**, *112*, E303−E310.
(58) Celeghini, E. C. C.; Alves, M. B. R.; de Arruda, R. P.; de Rezende, G. M.; Florez-Rodriguez, S. A.; de Sá Filho, M. F. Efficiency of CellROX deep red® and CellROX orange® fluorescent probes in identifying reactive oxygen species in sperm samples from high and low fertility bulls. *Animal Biotechnology* **2021**, *32*, 77−83.
(59) Ahmad, T.; Aggarwal, K.; Pattnaik, B.; Mukherjee, S.; Sethi, T.; Tiwari, B. K.; Kumar, M.; Micheal, A.; Mabalirajan, U.; Ghosh, B.; Roy, S. S.; Agrawal, A. Computational classification of mitochondrial shapes reflects stress and redox state. *Cell Death Dis.* **2013**, *4*, No. e461.
(60) Hussain, H.; Santhana, R. L.; Ahmad, S.; Abd Razak, M. F.; Mohamud, W. N. W.; Bakar, J.; Ghazali, H. M. Determination of cell viability using acridine orange/propidium iodide dual−spectrofluorometry assay. *Cogent Food Agric.* **2019**, *5*, No. 1582398.
(61) Kanzawa, T.; Germano, I. M.; Komata, T.; Ito, H.; Kondo, Y.; Kondo, S. Role of autophagy in Temozolomide−induced cytotoxicity for malignant glioma cells. *Cell Death & Differentiation* **2004**, *11*, 448−457.
(62) McMahon, R. J. Chemical Reactions Involving Quantum Tunneling. *Science* **2003**, *299*, 833−834.
(63) Feng, R.; Zhang, X.; Murugesan, V.; Hollas, A.; Chen, Y.; Shao, Y.; Walter, E.; Wellala, N. P. N.; Yan, L.; Rosso, K. M.; Wang, W. Reversible ketone hydrogenation and dehydrogenation for aqueous organic redox flow batteries. *Science* **2021**, *372*, 836−840.

https://doi.org/10.1021/jacsau.4c00815
JACS Au 2024, 4, 4856−4865